

Article

Improvement of Ice Surface Temperature Retrieval by Integrating Landsat 8/TIRS and Operation IceBridge Observations

Lijuan Song ^{1,2,†}, Yifan Wu ^{1,2,†}, Jiaying Gong ^{1,2} , Pei Fan ³ , Xiaopo Zheng ¹ and Xi Zhao ^{1,2,*} 

¹ School of Geospatial Engineering and Science, Sun Yat-sen University, and Southern Marine Science and Engineering Guangdong Laboratory (Zhuhai), Zhuhai 519000, China; songlj7@mail2.sysu.edu.cn (L.S.); wuyf235@mail2.sysu.edu.cn (Y.W.); gongjx7@mail2.sysu.edu.cn (J.G.); zhengxp28@mail.sysu.edu.cn (X.Z.)

² Key Laboratory of Comprehensive Observation of Polar Environment (Sun Yat-sen University), Ministry of Education, Zhuhai 519082, China

³ National Marine Environmental Monitoring Center, Dalian 116023, China; fan_pei@outlook.com

* Correspondence: zhaoxi6@mail.sysu.edu.cn

† These authors contributed equally to this work.

Abstract: Accurate retrieval of ice surface temperature (IST) over the Arctic ice-water mixture zone (IWMZ) is significantly essential for monitoring the change of the polar sea ice environment. Previous researchers have focused on evaluating the accuracy of IST retrieval in pack ice regions, possibly on account of the availability of in situ measurement data. Few of them have assessed the accuracy of IST retrieval on IWMZ. This study utilized Landsat 8/TIRS and Operation IceBridge observations (OIB) to evaluate the accuracy of the current IST retrieval method in IWMZ and proposed an adjustment method for improving the overall accuracy. An initial comparison shows that Landsat 8 IST and OIB IST have minor differences in the pack ice region with RMSE of 0.475 K, MAE of 0.370 K and cold bias of -0.256 K. In the thin ice region, however, the differences are more significant, with RMSE of 0.952 K, MAE of 0.776 K and warm bias of 0.703 K. We suggest that this phenomenon is because the current ice-water classification method misclassified thin ice as water. To address this issue, an adjusted method is proposed to refine the classification of features within the IWMZ and thus improve the accuracy of IST retrieval using Landsat 8 imagery. The results demonstrate that the accuracy of the retrieved IST in the two cases was improved in the thin ice region, with RMSE decreasing by about 0.146 K, Bias decreasing by about 0.311 K, and MAE decreasing by about 0.129 K. After the adjustment, high accuracy was achieved for both pack ice and thin ice in IWMZ.

Keywords: ice surface temperature (IST); Landsat 8/TIRS; Operation IceBridge (OIB); ice-water classification



Citation: Song, L.; Wu, Y.; Gong, J.; Fan, P.; Zheng, X.; Zhao, X. Improvement of Ice Surface Temperature Retrieval by Integrating Landsat 8/TIRS and Operation IceBridge Observations. *Remote Sens.* **2023**, *15*, 4577. <https://doi.org/10.3390/rs15184577>

Academic Editors: Yubao Qiu, Tonghua Wu, Florent Garnier and Lin Liu

Received: 2 August 2023

Revised: 9 September 2023

Accepted: 14 September 2023

Published: 17 September 2023



Copyright: © 2023 by the authors. Licensee MDPI, Basel, Switzerland. This article is an open access article distributed under the terms and conditions of the Creative Commons Attribution (CC BY) license (<https://creativecommons.org/licenses/by/4.0/>).

1. Introduction

During the past 40 years, the extent, thickness, and volume of Arctic sea ice have declined, while the ice surface temperature (IST) has been consistently rising [1–3]. IST is one of the crucial factors for evaluating climate change, reflecting alterations in the surface energy balance that control ice formation rates, ice melting, and heat exchange between the ocean and atmosphere [4,5]. Owing to the extreme cold and complex environmental conditions in the Arctic, few in situ measurements are available [6,7]. Compared with traditional in situ measurements, remote sensing technology has the advantages of low cost, wide coverage, and rapid updating. The emergence of remote sensing techniques has facilitated the detection of changes occurring on the Earth on a steady basis, such as monitoring the variation of Arctic sea ice and providing an opportunity to gain a deeper insight into surface temperature changes in the Arctic [8–11].

Many scholars have studied surface temperature retrieval within the Arctic sea ice region utilizing thermal infrared imagery acquired by satellite-borne thermal infrared

sensors, such as Terra and Aqua/moderate resolution imaging spectroradiometer (MODIS), advanced very high-resolution radiometer (AVHRR), and advanced spaceborne thermal emission and reflection radiometer (ASTER), etc., to improve the understanding of climate change in the Arctic [9,11–14]. Surface temperature quantification in the Arctic ice-water mixture zone (IWMZ) faces several challenges due to large inter-annual and intra-annual fluctuations in sea ice coverage and the complexity of the sea ice and water mixture [15,16]. Mixed pixels in MODIS or AVHRR imagery (coarser spatial resolution) may cover sea ice and open water near the sea ice edge, leads, or melt ponds (in summer), diminishing the precision of IST retrieval in the IWMZ [14]. Hence, it is crucial to develop appropriate IST retrieval methods in the IWMZ from images with finer spatial resolution. Hall et al. [17] and Son et al. [18] assessed the accuracy of IST retrieval approaches by utilizing Landsat 7 and ASTER in Greenland and the Arctic Ocean coast. The Landsat 8 is equipped with two thermal infrared bands (bands 10 and 11) on a thermal infrared sensor (TIRS), which is anticipated to outperform its predecessor. Yet, the understanding of the accuracy of IST retrieval using Landsat imagery in the IWMZ is still limited due to the difficulty of collecting time-matched in situ measured data.

Different surface temperature retrieval algorithms based on satellite-based thermal infrared images have been developed [19–27]. Among them, the split-window algorithm (SW) is more extensively employed than the single-channel algorithm (SC) to retrieve surface temperature because it is simple to operate and necessitates fewer supportive parameters to correct atmospheric influences. The SW algorithm has become the standard IST retrieval method for low- and moderate-resolution images such as AVHRR and MODIS data [13,28,29]. Many previous studies have addressed the issue of IST product validation by comparing them with in situ observed surface temperatures. These satellite ISTs generally exhibit good agreement with in situ IST observations, with overall accuracy better than 3 K in most situations [8,14,18]. Fan et al. [8] quantified the overall accuracy of IST retrieved by five commonly used SW and SC methods according to Landsat 8 images in the Arctic and found that the SW algorithm proposed by Du et al. [22] (SW-Du) method performed the best. Therefore, this study utilized the SW-Du algorithm for IST retrieval from Landsat 8/TIRS images.

Previous researchers have demonstrated that in situ IST observations in the Arctic Ocean, such as ice mass balance buoy and automatic weather station data, are susceptible to environmental variations such as solar heating and snow cover [6]. The Operation IceBridge (OIB) project has acquired valuable surface temperature data through conducting airborne surveys in the Arctic during the years 2012–2014 and 2017–2019, providing an unprecedented opportunity to perform the validation of thin ice IST retrieval. Fan et al. [30] compared four dominant recording methods for Arctic IST and found that the airborne IST had the best accuracy. Whereas previous validation results based on buoys and automatic weather stations represent the accuracies mainly for the pack ice zone and seldom in the IWMZ.

The crucial objective of this study is to verify the accuracy of surface temperature retrieval for various typical surface features (pack ice, thin ice, and open water) in the IWMZ by integrating Landsat 8/TIRS and airborne surface temperature from OIB observations. In addition, we proposed an adjusted ice-water classification method to improve the accuracy of the thin ice temperature retrieval. The following sections of the manuscript are structured as follows. Section 2 describes the collection of Landsat 8 images and OIB IST observations matching the data in IWMZ. Section 3 explains the problems of thin ice temperature retrieval in IWMZ. Section 4 introduces the improvements in ice classification and the IST algorithm. The discussion and conclusions are in Sections 5 and 6.

2. Data and Preprocessing

2.1. Landsat 8 Imagery

Landsat 8 is an Earth observation satellite launched on 11 February 2013, carrying the Operational Land Imager and the Thermal Infrared Sensor (TIRS) [31]. The Operational Land Imager consists of nine bands (B1 to B9), including panchromatic band B8 (15 m) and

other bands of 30 m, while TIRS includes two 100 m TIR bands with wavelengths between 10.60 μm and 12.51 μm (B10 to B11). To match the Operational Land Imager images, the existing publicly accessible TIRS images were resampled to 30 m using a cubic convolution method [32]. The resampling operation of the TIRS band in Landsat 8 images is processed by the United States Geological Survey. In this work, two scenes of Landsat 8/TIRS imagery were used to evaluate the accuracy of satellite-based IST retrieval in IWMZ.

2.2. Airborne Surface Temperature from OIB Observations

OIB IST was gathered by a Heitronics KT-19.85 Series II Infrared Radiation Pyrometer aboard the airplane, which was observed at infrared frequency intervals similar to AHVRR Channel 4 (9.6–11.5 μm) [33]. The accuracy of the IST retrieved by OIB observations (typically with a resolution of 0.01 $^{\circ}\text{C}$) may be affected due to error sources such as cloud cover beneath the aircraft (OIB campaigns did not screen out potential cloud cover) and variations of ice emissivity. The OIB IST records were stored by the National Snow and Ice Data Center.

2.3. Matching of OIB Observations Data and Landsat 8 Imagery in IWMZ

This study thoroughly examined all airborne IST records (293 tracks) acquired by the OIB project within 2012–2014 and 2017–2019 to match intersected Landsat 8 imagery in IWMZ. In total, 45 scenes of Landsat 8 images intersected with OIB tracks. Ultimately, two OIB IST tracks that intersected Landsat 8 were selected to quantify the performance of Landsat 8 in retrieving IST in IWMZ, based on image quality (clear and cloud-free) and the time interval between Landsat 8 and OIB data (<3 h). The selected OIB satisfied the comparison and verification of various features in the IWMZ through pack ice and thin ice. Because OIB IST is point data and one pixel of a Landsat 8 image may correspond to 2–3 points, we made direct point-pixel matching and did not use the average process. Figure 1 shows the track of the airborne IST records obtained from OIB campaigns and the location of the Landsat 8 image used for this study.

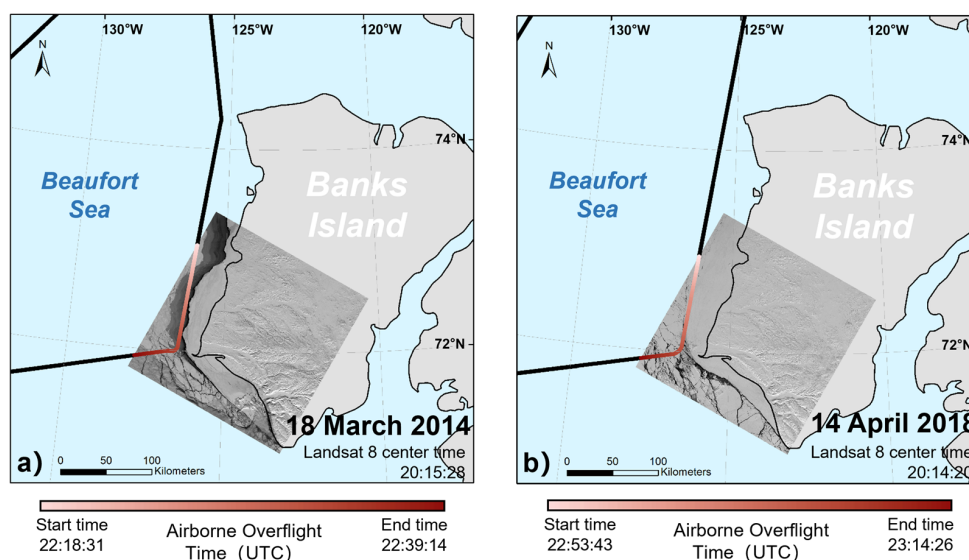


Figure 1. Spatial distribution of Landsat 8 imagery and OIB tracks (black is the OIB track, and red is the OIB track intersecting Landsat 8 image). (a) Landsat 8 image dated on 18 March 2014; (b) Landsat 8 image dated on 14 April 2018.

3. Methods

3.1. Split-Window (SW) Algorithm

The SW algorithm adopts different atmospheric absorption of two adjacent thermal infrared channels in the 10–12.5 μm window region to remove the atmospheric effect and

then utilizes the linear or non-linear combination of brightness temperature to achieve the retrieval of the surface temperature when the atmospheric profile is unknown [34]. Currently, the SW algorithm is recommended for retrieving land/sea/ice temperatures from infrared sensors aboard various satellite platforms. In this research, IST is derived from Landsat 8/TIRS images using the SW-Du algorithm. The SW-Du approach utilizes the MODIS surface temperature product model (Equation (1)), but with adjustments for specific constant parameters. Fan et al. [8] have recommended the SW-Du algorithm as the preferred method for estimating IST after comparing it with other temperature retrieval algorithms against in situ measurements from buoys and automatic weather stations. The constant b_i in Equation (1) is obtained by simulation with the help of MODTRAN software 5.2 and thermodynamic initial guess retrieval of the atmospheric profile, as described in Table 1. Further details of the SW-Du algorithm can be seen in Du et al. [22].

$$T_s = b_0 + \left(b_1 + b_2 \frac{1 - \epsilon}{\epsilon} + b_3 \frac{\Delta\epsilon}{\epsilon^2} \right) \frac{T_{10} + T_{11}}{2} + \left(b_4 + b_5 \frac{1 - \epsilon}{\epsilon} + b_6 \frac{\Delta\epsilon}{\epsilon^2} \right) \frac{T_{10} - T_{11}}{2} + b_7 (T_{10} - T_{11})^2 \tag{1}$$

where T_{10} and T_{11} are the two thermal infrared channels (band 10 and band 11) in the Landsat 8 image, respectively; ϵ means the average emissivity of two channels (i.e., $\epsilon = 0.5 \times (\epsilon_i - \epsilon_j)$); $\Delta\epsilon$ represents the difference of channel emissivity (i.e., $\Delta\epsilon = \epsilon_i - \epsilon_j$); b_i ($i = 0, 1, \dots, 7$) values are shown in Table 1.

Table 1. The constant b_i employed by SW-Du in Equation (1).

b_0	b_1	b_2	b_3	b_4	b_5	b_6	b_7
-0.41165	1.00522	0.14543	-0.27297	4.06655	-6.92512	-18.27461	0.24468

The channel-effective emissivity is derived from the TIRS spectral response function and the ASTER spectral library (accessed at <http://speclib.jpl.nasa.gov/> (accessed on 8 July 2023)) [35]. Table 2 shows the emissivity of various features that may be present in the IWMZ for IST retrieval. Notably, snow utilizes the average emissivity of different snow types because the type of snow on the ice surface is unclear [8]. According to Table 2, the ϵ and $\Delta\epsilon$ of different types for IST retrieval in Equation (1) can be obtained in the IWMZ.

Table 2. Emissivity values for IST retrieval derived from ASTER spectral library.

TIRS Channel	Sea Water	Coarse Snow	Medium Snow	Fine Snow	Bare Ice
Band 10	0.991	0.9851	0.9907 Average of Snow: 0.990	0.9951	0.987
Band 11	0.986	0.963	0.98 Average of Snow: 0.978	0.9896	0.954

3.2. The Traditional Ice-Water Classification Method

This study first adopted a combination of the normalized difference snow index (NDSI) and the reflectance of the near-infrared band (NIR) for snow/ice and water classification, as used in Macander et al. [36] and Fan et al. [8]. Before calculating the NDSI index, we converted the digital number values to reflectance values. According to Landsat 8 images, the top of the atmosphere reflectance of channel 3 (green band) and channel 6 (SWIR band) are selected to calculate NDSI: $NDSI = (b_3 - b_6)/(b_3 + b_6)$. Pixels with NDSI values greater than 0.4 and NIR values greater than 0.11 are categorized as snow/ice, whereas pixels with positive NDSI values but not classified as snow/ice were classified as water (such as open water, ice-free leads, or waterlogged ice surfaces) [8,37,38].

3.3. The Adjusted Ice-Water Classification Method

In the IWMZ, thin ice was misclassified as water based on the ice-water classification by the combination of NDSI and NIR, resulting in the emissivity of water being used for IST retrieval in thin ice regions. As shown in Section 4, this situation affects the accuracy of the IST calculation and increases the error in the thin ice zones (refrozen ice, newly formed ice, etc.). To more accurately extract “true water” in the IWMZ and reduce the probability of misidentifying thin ice as water, the ice-water classification method needs to be adjusted. We propose to introduce the normalized difference water index (NDWI) to address this issue.

The NDWI index utilizes a combination of near-infrared and green bands to enhance the information for water bodies in the green band while minimizing non-water bodies in the NIR band [39]. For Landsat 8 images, channel 3 (green band) and channel 5 (NIR band) were selected to calculate NDWI: $NDWI = (b3 - b5)/(b3 + b5)$. In most cases, NDWI has been proven to be effective in enhancing water-related information [40,41]. This study used the classification algorithm combined by NDSI and NDWI, which is called the adjusted ice-water classification method. The specific thresholds of NDSI and NDWI in the adjusted ice-water classification method were determined in Sections 4.2 and 4.3.

4. Results

4.1. Accuracy Assessment of Surface Temperature Retrieval Based on Landsat IST and OIB IST in IWMZ

We compared the Landsat 8 IST retrieved via the SW-Du algorithm with the OIB IST. The differences are estimated by using three evaluation metrics, namely root mean square error (RMSE), mean predictive bias (Bias), and mean absolute error (MAE), to investigate the performance of IST retrieval. Figure 2 shows the difference in visualization and residual histograms for the IST of pack ice (a and b) and thin ice (c and d). The Landsat 8 IST and OIB IST in pack ice exhibited high consistency (Figure 2b), with RMSE, Bias, and MAE reaching 0.475 K, -0.256 K, and 0.370 K, respectively. Whereas the deviation is relatively large in the thin ice region (Figure 2d), with RMSE, Bias, and MAE of 0.952 K, 0.703 K, and 0.776 K, respectively. Therefore, we further explore why the IST retrieval error of thin ice is more significant in the IWMZ and attempt to improve the IST retrieval accuracy.

Accurate emissivity estimation is essential for obtaining reliable surface temperature results. The emissivity of water, snow, and ice within the IWMZ has specific differences in the thermal infrared band, and the emissivity of ice resembles that of snow in the thermal infrared band. Thus, the surface type classification before the IST retrieval should be as accurate as possible. According to OIB IST and the synchronous high-resolution optical image from the digital mapping system (DMS) acquired by OIB flights, we found that a large amount of thin ice in the Landsat 8 image in winter was misclassified as water based on the traditional ice-water classification method (Figure 3).

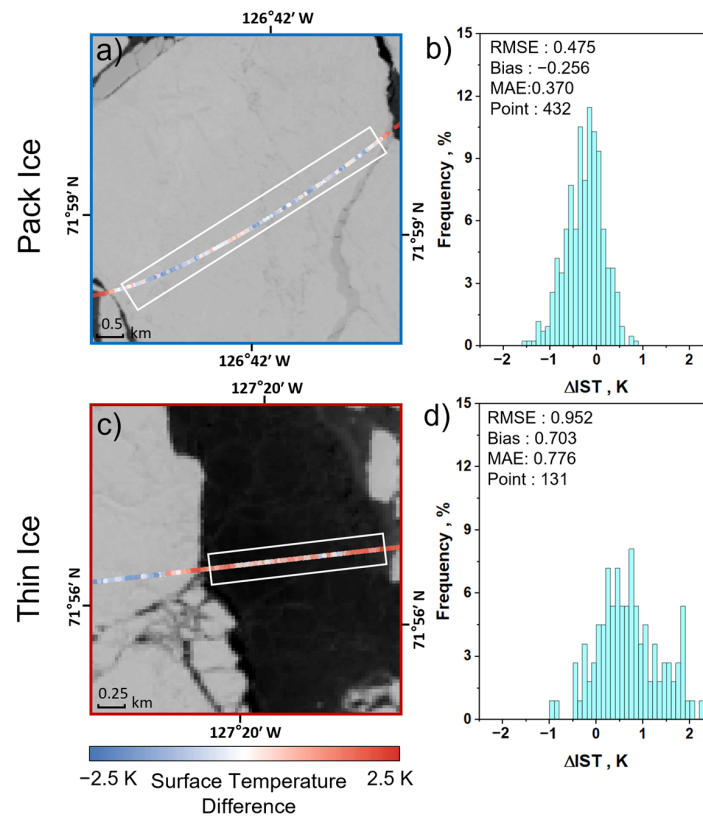


Figure 2. Deviation visualization and histograms for the IST of pack ice (a,b) and thin ice (c,d). The color bar (a,c) represents the temperature difference between Landsat 8 IST and OIB IST. White rectangles are cropped regions for comparison. The date of the Landsat 8 image is 14 April 2018, and the OIB time at the center point for the white rectangle of (a) is 23:12:28 (UTC), while the (c) is 23:09:01 (UTC).

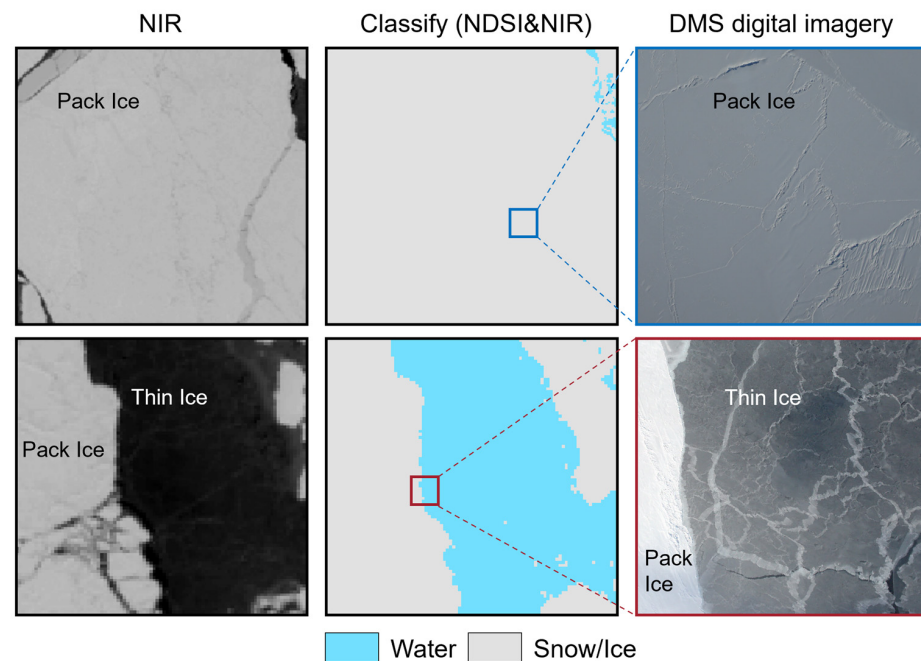


Figure 3. Snow/ice and water distribution in the pack and thin ice regions classified by NDSI and NIR (second column image) and visible data of DMS digital imagery from OIB campaigns on the same date (third column image).

4.2. Improvement of Ice Classification Case 1: Landsat 8 Image Dated 14 April 2018

We took the matching data from OIB IST and Landsat 8 images on 14 April 2018 as the first case. Firstly, Landsat 8 image pixels were randomly sampled from three categories classified in Section 3: Pack ice, thin ice, and water by visual interpretation. Next, for these samples, a scatter density plot was created to determine the distinguishability of three categories in the space of NDSI and NIR. Results show that the previous algorithm using NDSI (with a threshold of 0.4) and NIR (threshold of 0.11) tends to classify both thin ice and water as water (Figure 4a,b). In Case 1, pack ice was well extracted using a NIR threshold greater than 0.11, but less than this threshold, both thin ice and water were classified as water (Figure 4a). However, the proximity of bimodal distribution intervals (Figure 4b) made it challenging to differentiate between thin ice and water using NIR. Figure 4c shows the density scatter plot constructed by the combined NDSI and NDWI indices, and the points on this scatter plot correspond to the same sampling pixels as before, with three distinct clusters corresponding to pack ice, thin ice, and water, respectively. Compared with Figure 4a, the three types of pack ice, thin ice, and water have a higher degree of discrimination in Figure 4b. Figure 4d has three distinct peaks. The first peak corresponds to pack ice, and the thin ice and water below correspond to the remaining two peaks, respectively. The thin ice and water can be differentiated based on the distance between the two peaks, utilizing the NDWI threshold of 0.3. Combined with the threshold for NIR extraction of pack ice (NIR greater than 0.11), this study classified pixels with NIR less than 0.11 and NDWI greater than 0.3 as thin ice. Figure 5 presents the classification results of Landsat 8 imagery on 14 April 2018, as well as the temperature estimations for water and thin ice using the adjusted ice-water classification method. Comparisons show that applying NDWI to ice-water classification significantly reduces the extent of the water body while accurately distinguishing thin ice (as shown in Figure 5b,c). Furthermore, the surface temperature retrieved by the adjusted ice-water classification method based on Landsat 8/TIRS ranges from 256 K to 274 K (Figure 5d), which is highly consistent with the ice-water classification results (Figure 5c).

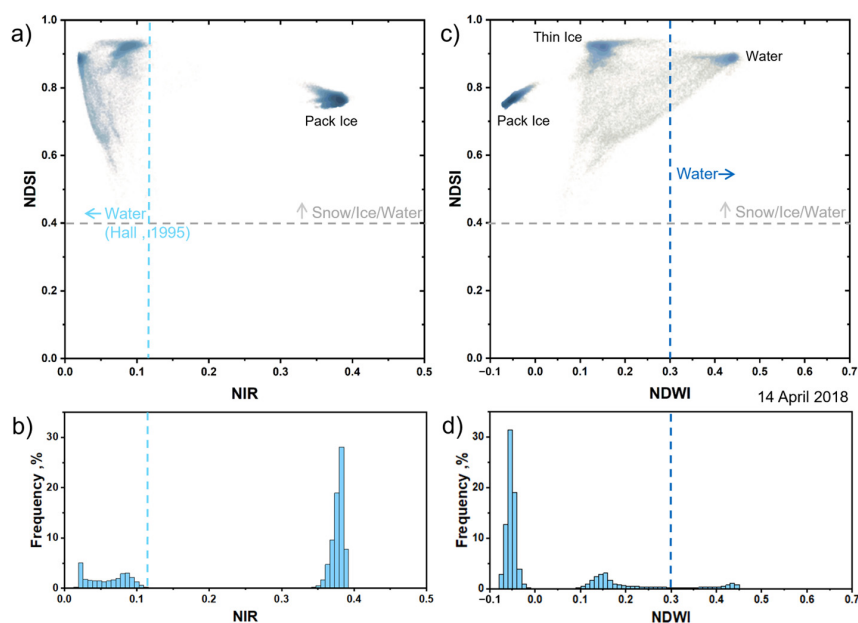


Figure 4. Density scatterplot and its probability distribution constructed from Landsat 8 image classification results. (a,b) Based on the ice-water classification by the combination of NDSI and NIR [37]; (c,d) based on the ice-water classification by the combination of NDSI and NDWI. The bright blue line is the threshold used by NIR (threshold of 0.11) to classify water bodies; the gray line indicates the threshold utilized by NDSI (with a threshold of 0.4) to classify snow/ice; and the dark blue line represents the threshold adopted by NDWI (with a threshold of 0.3) to classify water bodies.

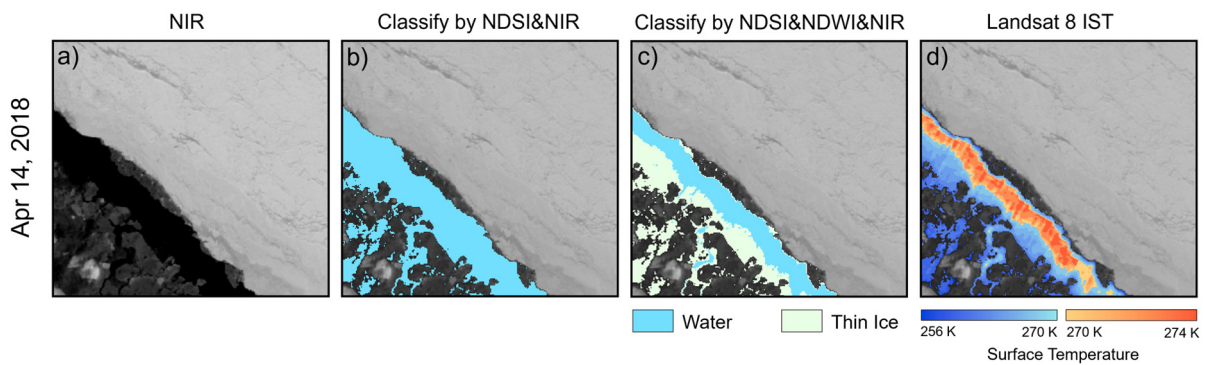


Figure 5. Classification results for thin ice and water in the non-thick ice region on 14 April 2018 using different combinations of NDSI, NDWI, and NIR ice-water classification methods (a–c) and the surface temperature maps derived from Landsat 8/TIRS (d), which were retrieved by (c) adjusted classification result.

After correcting the misclassified water body as thin ice, the thin ice temperature at the OIB track improved (Figure 6), consistent with the surface temperatures detected by the OIB observations (259–262 k). According to the DMS image in Figure 2, thin ice does not belong to bare ice, so the emissivity of snow is used for temperature retrieval instead of water, which was initially adopted. The improved Landsat 8 IST has better consistency with OIB IST, with an RMSE of 0.749 K (21% better than 0.952 K), a Bias of 0.333 K (52% better than 0.703 K), and an MAE of 0.586 K (24% better than 0.776 K), as shown in Table 3. The consequences indicate that the proposed new approach increases the accuracy of IST retrieval from Landsat 8 images, especially for the non-thick ice regions (such as thin ice and leads) in IWMZ.

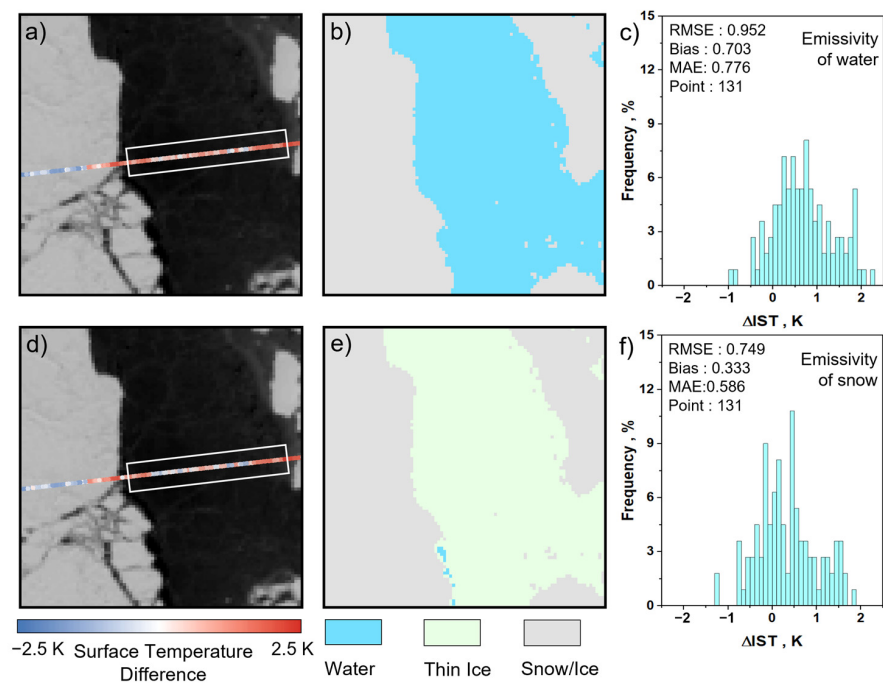


Figure 6. Deviation visualization (a,d), ice-water classification distribution (b,e) and deviation histograms (c,f) for IST retrieval based on Landsat 8 imagery using the adjusted ice-water classification results. The first row shows the Landsat IST versus the OIB IST derived from the previous classification method (a–c). The second row compares Landsat IST and OIB IST derived from the adjusted ice-water classification method (d–f).

Table 3. Accuracy of IST retrieved using Landsat 8 images based on different ice-water classification methods compared with OIB IST.

	Landsat IST vs. OIB IST		
	RMSE (K)	Bias (K)	MAE (K)
Landsat IST obtained from the old ice-water classification method	0.952	0.703	0.776
Landsat IST derived from the adjusted ice-water classification method	0.749	0.333	0.586

4.3. Improvement of Ice Classification Case 2: Landsat 8 Image Dated 18 March 2014

To verify the generalizability of the adjusted ice-water classification algorithm, matching data from another scene of Landsat 8 imagery (dated on 18 March 2014) and OIB IST were selected for validation analysis as Case 2. Figure 7 shows the density scatter plot and probability density plot for the three types of features: Pack ice, thin ice, and water. Three types of features (water, thin ice, and pack ice) all clustered (as shown in Figure 7a) with a high degree of separability, consistent with Case 1 (Figure 4c). Three peaks in the probability density plot, which correspond to the three clustered regions on the density scatterplot, indicate that utilizing 0.3 as the threshold of NDWI to delineate thin ice and water is reliable. Applying a combined classification method with NDSI greater than 0.4 and NDWI greater than 0.3 again effectively extracts water. The ice-water classification results in IWMZ obtained by applying different parameter combinations and the corresponding IST derived from Landsat 8/TIRS are shown in Figure 8. By comparing the near-infrared images in Figure 8, we can see that the water extracted based on the previous method misclassifies thin ice into water, whereas our proposed method made a significant improvement in the ice-water classification. The proposed method further distinguishes thin ice from water, and the estimated water surface temperature is above 270 K. From the visual interpretation of Figure 8, it can be found that the temperature distributions of water and thin ice are in high agreement with the classification results of ice-water, which is consistent with the conclusion from Case 1.

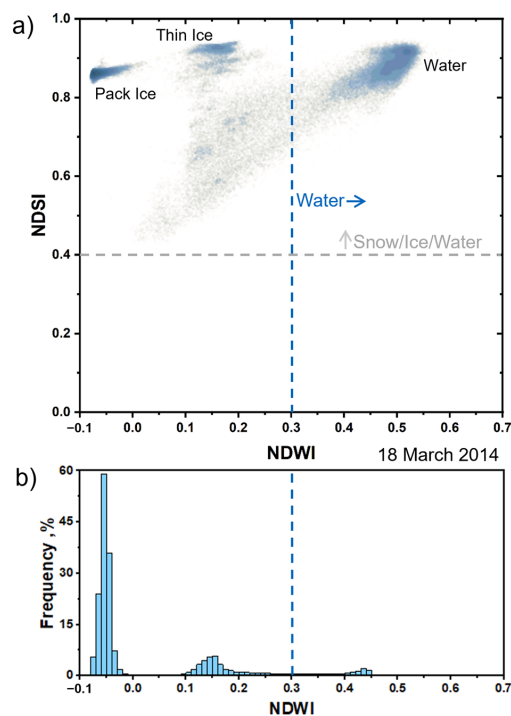


Figure 7. Scatter density plot (a) and its probability density plot (b) are constructed by combining NDWI and NDSI. Pixels with NDSI greater than 0.4 (gray line) and NDWI greater than 0.3 (dark blue line) were identified as water.

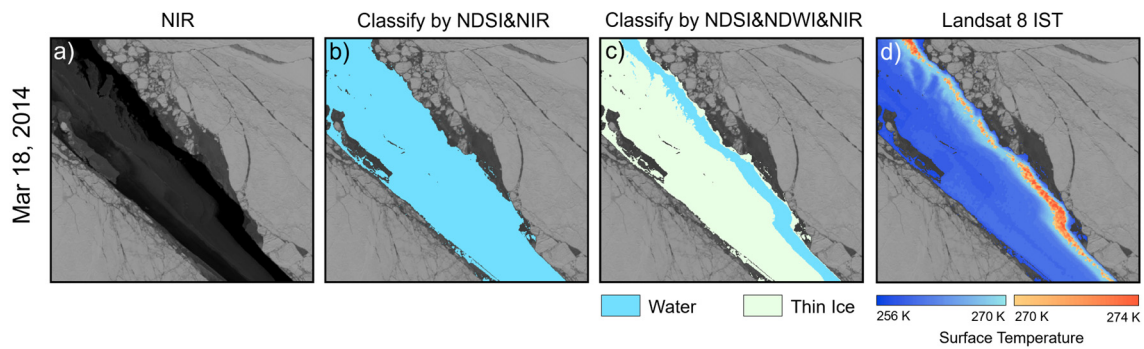


Figure 8. Classification results for thin ice and water in the non-thick ice area on 18 March 2014 using different combinations of NDSI, NDWI, and NIR ice-water classification methods (a–c) and the surface temperature maps derived from Landsat 8/TIRS (d), which were retrieved by (c) adjusted classification result.

For Case 2, the deviation histogram obtained by comparing the IST retrieved from the Landsat 8 image with the OIB IST is shown in Figure 9. Landsat 8 IST has a minor error compared to OIB IST for thick ice, with an RMSE of 0.584 K, an MAE of 0.458 K, and a Bias of -0.133 K (Figure 9a). On thin ice, the IST estimated using Landsat 8 imagery based on the previous method has higher accuracy than the IST based on the adjusted method, with an RMSE of 0.918 K, an MAE of 0.713 K, and a Bias of 0.392 K. The Bias of IST retrieval using either water or snow emissivity is positive in thin ice regions, indicating that Landsat 8 IST overestimates surface temperature compared to validation data (OIB IST).

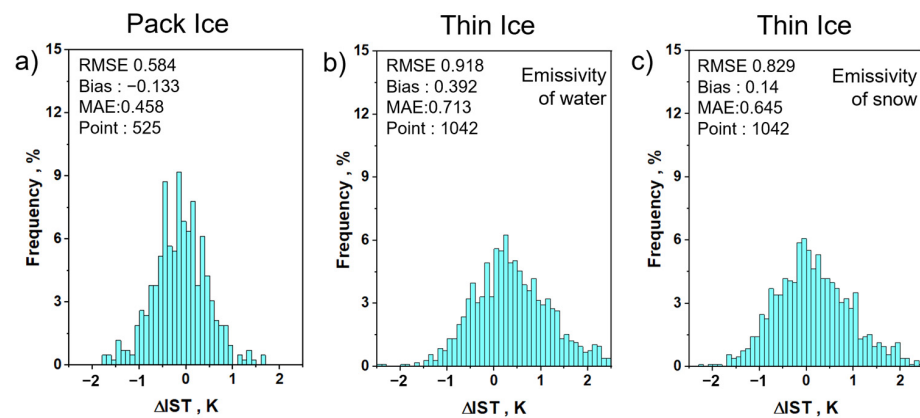


Figure 9. Histogram of difference between the surface temperature retrieved by Landsat 8 and the temperature measured by OIB. (a) The deviation between OIB IST and Landsat 8 IST estimated by the snow emissivity for pack ice; (b) deviation between OIB IST and Landsat 8 IST estimated by the water emissivity for thin ice (based on the previous method); (c) deviation between OIB IST and Landsat 8 IST estimated by the snow emissivity for thin ice (based on the adjusted method).

5. Discussion

5.1. Comparison of Different Algorithms for IST Retrieval

The SC algorithm is also widely used for IST retrieval. For satellite images with one thermal infrared channel, surface temperature retrieval can only be performed through the SC algorithm. In this research, we applied SC presented by Barsi et al. [42] (SC-Barsi) to retrieve IST from Landsat 8 images employing Band 10 or Band 11 imagery for comparison with the IST estimated by the SW-Du algorithm. Barsi et al. [42] and Barsi et al. [43] contributed the online atmospheric correction website (<https://atmcorr.gsfc.nasa.gov/>) (accessed on 8 July 2023) to dwindle the laborious operation of estimating atmospheric parameters based on Landsat series images in the case of a small amount of data. SC-Barsi supposes that the atmospheric parameters of the whole image do not change

significantly and then calculates atmospheric parameters based on satellite elapsed time and the position of the image with the help of atmospheric global profiles simulated by the National Centers for Environmental Prediction and the MODTRAN code. We selected pixels in the two Landsat 8 images that matched the OIB IST point data to evaluate the IST retrieval accuracy of SW-Du and SC-Barsi in thin ice and thick ice. Results indicate that the IST derived from the SW-Du algorithm and the OIB IST have higher consistency (as illustrated in Figure 10), with RMSE, Bias, and MAE of 0.971 K, 0.224 K, and 0.754 K on thin ice and RMSE, Bias, MAE of 0.841 K, -0.399 K, and 0.694 K on pack ice. In other words, the SW algorithm shows better accuracy than the SC method at our experiment sites.

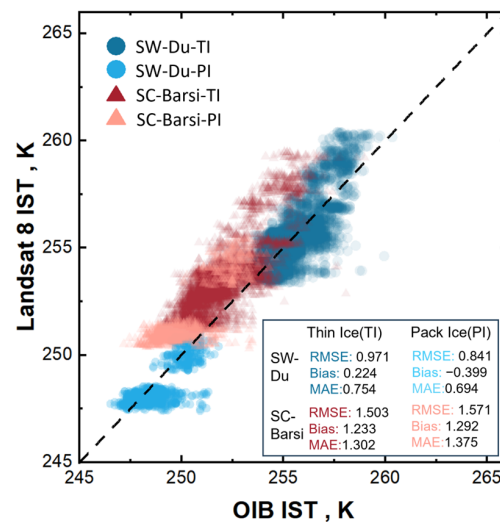


Figure 10. Scatter plots of OIB IST against Landsat IST retrieved from SW-Du and SC-Barsi algorithms for thin ice and pack ice.

Regarding the selection of emissivity for the thin ice, we checked the ice types in the thin ice regions passed by the two OIB tracks based on airborne DMS digital imagery and found no bare ice present. Nonetheless, we also tested the emissivity of bare ice on thin ice for comparison. The difference between Landsat 8 IST and OIB IST presents a significant cold bias (Figure 11), with RMSE, Bias, and MAE of 1.069 k, -0.836 k, and 0.919 k, respectively. Because bare ice seldom occurs in the Arctic winter, the combined NDSI and NDWI ice-water classification method is recommended for the IWMZ in Arctic winters to categorize thin ice and pack ice as one category and water as another. In summary, IST retrieval results calculated using snow emissivity for thin and pack ice are more accurate.

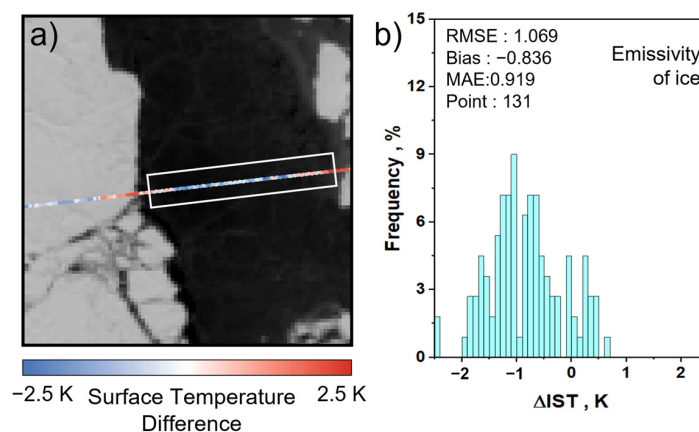


Figure 11. Deviation visualization (a) and histograms (b) for the IST of thin ice using the emissivity of bare ice.

5.2. Comparison of the IST Retrieval with Previous Relevant Studies

Based on multi-source remote sensing imagery, many prior studies have used different IST retrieval algorithms to elucidate the IST variation characteristics in the Arctic region [8,13,18,30,44,45]. For example, Li et al. [26] proposed an improved SC algorithm based on the radiative transfer equation for IST retrieval derived from band 10 of Landsat-8 images. Fan et al. [8] evaluated the accuracy of three SW and two SC methods based on Landsat 8/TIRS imagery over the Arctic sea ice region. However, owing to the high variability of sea ice coverage and the complexity of the ice-water mixture within the IWMZ, there is still a lack of assessment of the accuracy of IST retrieval in the IWMZ. By integrating Landsat 8/TIRS and airborne IST obtained from OIB observation data, this research evaluated the accuracy of surface temperature retrieval of various typical ground objects in the IWMZ and found that the accuracy of IST retrieval in the thin ice region was relatively low. To improve the accuracy of IST retrieval on thin ice, we proposed the adjusted ice-water classification method. The adjusted ice-water classification method combines NDSI and NDWI to correctly distinguish thin ice from IWMZ. This classification method requires images with an SWIR band, NIR band, and green band, which can be applied to commonly used MODIS and Sentinel-2 images.

Along with the IST retrieval deviation caused by ice-water classification error, the selection of the IST retrieval algorithm, image spatial resolution, and atmospheric environment are also crucial factors affecting the accuracy of IST retrieval [8,45]. Using this classification method at a relatively coarse spatial resolution (250 m or 1 km) may lead to biased mapping results due to the mixed-pixel problem. Clouds and sea ice have similar reflective characteristics at visible wavelengths, which makes it difficult to remove small clouds and fog, thus affecting the accuracy of sea ice classification [18]. In this study, we selected clear and cloudless Landsat 8 images with high spatial resolution for IST retrieval by visual interpretation.

6. Conclusions

This study compared OIB IST data and Landsat 8/TIRS IST data to evaluate the current IST retrieval method. We found that there is good uniformity between the satellite-retrieved IST and the airborne IST, and the Bias, RMSE, and MAE between the Landsat 8 IST and the OIB IST are all within 1 K. The IST of pack ice has higher accuracy than that of thin ice, possibly because the current method misclassifies the thin ice regions as water and assigns the emissivity of water in the IST retrieval. The adjusted ice-water classification method combining NDWI and NDSI was proposed in this study. Open water and frozen sea ice can be classified utilizing the adjusted algorithm with NDSI greater than 0.4 and NDWI greater than 0.3. Based on the corrected classification results, the emissivity of water was assigned for the water body region, and the emissivity of snow was assigned for thin ice and pack ice. The IST accuracy of the thin ice region retrieved from the two Landsat 8 images in Case 1 and Case 2 was improved, with RMSE decreasing by about 0.146 K, Bias decreasing by about 0.311 K, and MAE decreasing by about 0.129 K. The method of introducing NDWI for ice-water classification presented in this research can be generalized to other satellite images to correctly classify ice and water and enhance the accuracy of IST retrieval using remote sensing images in polar regions.

Author Contributions: Conceptualization, X.Z. (Xi Zhao) and L.S.; methodology, X.Z. (Xi Zhao), L.S., Y.W. and J.G.; data curation, L.S. and Y.W.; writing—original draft, L.S., Y.W. and J.G.; writing—review and editing L.S., X.Z. (Xi Zhao), P.F., J.G. and X.Z. (Xiaopo Zheng); supervision, X.Z. (Xi Zhao), P.F. and X.Z. (Xiaopo Zheng); visualization, L.S., Y.W. and J.G.; funding acquisition, X.Z. (Xi Zhao); project administration, X.Z. (Xi Zhao). All authors have read and agreed to the published version of the manuscript.

Funding: This research was funded by the National Key Research and Development Program of China (Grant No. 2021YFC2801300), the Innovation Group Project of Southern Marine Science and Engineering Guangdong Laboratory (Zhuhai) (Grant No. 311022003), and the National Natural Science Foundation of China (Grant No. 42101347).

Acknowledgments: The authors express their gratitude to the National Aeronautics and Space Administration (NASA) for providing the Landsat 8 images and the ice surface temperature data from the Operation IceBridge (OIB) observations.

Conflicts of Interest: The authors declare no conflict of interest.

References

1. Comiso, J.C.; Meier, W.N.; Gersten, R. Variability and trends in the Arctic Sea ice cover: Results from different techniques. *J. Geophys. Res. Ocean.* **2017**, *122*, 6883–6900. [[CrossRef](#)]
2. Kwok, R. Arctic sea ice thickness, volume, and multiyear ice coverage: Losses and coupled variability (1958–2018). *Environ. Res. Lett.* **2018**, *13*, 105005–105015. [[CrossRef](#)]
3. Cavalieri, D.J.; Parkinson, C.L. Arctic sea ice variability and trends, 1979–2010. *Cryosphere* **2012**, *6*, 881–889. [[CrossRef](#)]
4. Koo, Y.; Lei, R.; Cheng, Y.; Cheng, B.; Xie, H.; Hoppmann, M.; Kurtz, N.T.; Ackley, S.F.; Mestas-Núñez, A.M. Estimation of thermodynamic and dynamic contributions to sea ice growth in the Central Arctic using ICESat-2 and MOSAiC SIMBA buoy data. *Remote Sens. Environ.* **2021**, *267*, 112730. [[CrossRef](#)]
5. Fichefet, T.; Maqueda, M.A.M. Sensitivity of a global sea ice model to the treatment of ice thermodynamics and dynamics. *J. Geophys. Res. Ocean.* **1997**, *102*, 12609–12646. [[CrossRef](#)]
6. Hall, D.K.; Nghiem, S.V.; Rigor, I.G.; Miller, J.A. Uncertainties of Temperature Measurements on Snow-Covered Land and Sea Ice from In Situ and MODIS Data during BROMEX. *J. Appl. Meteorol. Clim.* **2015**, *54*, 966–978. [[CrossRef](#)]
7. Supply, A.; Boutin, J.; Kolodziejczyk, N.; Reverdin, G.; Lique, C.; Vergely, J.L.; Perrot, X. Meltwater Lenses Over the Chukchi and the Beaufort Seas During Summer 2019: From In Situ to Synoptic View. *J. Geophys. Res. Ocean.* **2022**, *127*, e2021JC018388. [[CrossRef](#)]
8. Fan, P.; Pang, X.; Zhao, X.; Shokr, M.; Lei, R.; Qu, M.; Ji, Q.; Ding, M. Sea ice surface temperature retrieval from Landsat 8/TIRS: Evaluation of five methods against in situ temperature records and MODIS IST in Arctic region. *Remote Sens. Environ.* **2020**, *248*, 111975–111990. [[CrossRef](#)]
9. Vincent, R.F. The Case for a Single Channel Composite Arctic Sea Surface Temperature Algorithm. *Remote Sens.* **2019**, *11*, 2393. [[CrossRef](#)]
10. Zheng, X.; Hui, F.; Huang, Z.; Wang, T.; Huang, H.; Wang, Q. Ice/Snow Surface Temperature Retrieval From Chinese FY-3D MERSI-II Data: Algorithm and Preliminary Validation. *IEEE Trans. Geosci. Remote Sens.* **2022**, *60*, 4512715. [[CrossRef](#)]
11. Comiso, J.C.; Cavalieri, D.J.; Markus, T. Sea ice concentration, ice temperature, and snow depth using AMSR-E data. *IEEE Trans. Geosci. Remote Sens.* **2003**, *41*, 243–252. [[CrossRef](#)]
12. Key, J.; Haefliger, M. Arctic ice surface temperature retrieval from AVHRR thermal channels. *J. Geophys. Res. Atmos.* **1992**, *97*, 5885–5893. [[CrossRef](#)]
13. Hall, D.K.; Key, J.R.; Case, K.A.; Riggs, G.A.; Cavalieri, D.J. Sea ice surface temperature product from MODIS. *IEEE Trans. Geosci. Remote Sens.* **2004**, *42*, 1076–1087. [[CrossRef](#)]
14. Scambos, T.A.; Haran, T.M.; Massom, R. Validation of Avhrr and Modis ice Surface temperature products using in Situ radiometers. *Ann. Glaciol.* **2006**, *44*, 345–351. [[CrossRef](#)]
15. Qu, M.; Pang, X.; Zhao, X.; Zhang, J.; Ji, Q.; Fan, P. Estimation of turbulent heat flux over leads using satellite thermal images. *Cryosphere* **2019**, *13*, 1565–1582. [[CrossRef](#)]
16. Zhang, J.; Schweiger, A.; Steele, M.; Stern, H. Sea ice floe size distribution in the marginal ice zone: Theory and numerical experiments. *J. Geophys. Res. Ocean.* **2015**, *120*, 3484–3498. [[CrossRef](#)]
17. Hall, D.; Box, J.; Casey, K.; Hook, S.; Shuman, C.; Steffen, K. Comparison of satellite-derived and in-situ observations of ice and snow surface temperatures over Greenland. *Remote Sens. Environ.* **2008**, *112*, 3739–3749. [[CrossRef](#)]
18. Son, Y.-S.; Kim, H.-c.; Lee, S. ASTER-Derived High-Resolution Ice Surface Temperature for the Arctic Coast. *Remote Sens.* **2018**, *10*, 662. [[CrossRef](#)]
19. Qin, Z.; Karnieli, A.; Berliner, P. A mono-window algorithm for retrieving land surface temperature from Landsat TM data and its application to the Israel-Egypt border region. *Int. J. Remote Sens.* **2001**, *22*, 3719–3746. [[CrossRef](#)]
20. Wang, F.; Qin, Z.; Song, C.; Tu, L.; Karnieli, A.; Zhao, S. An Improved Mono-Window Algorithm for Land Surface Temperature Retrieval from Landsat 8 Thermal Infrared Sensor Data. *Remote Sens.* **2015**, *7*, 4268–4289. [[CrossRef](#)]
21. Cristóbal, J.; Jiménez-Muñoz, J.; Prakash, A.; Mattar, C.; Skoković, D.; Sobrino, J. An Improved Single-Channel Method to Retrieve Land Surface Temperature from the Landsat-8 Thermal Band. *Remote Sens.* **2018**, *10*, 431. [[CrossRef](#)]
22. Du, C.; Ren, H.; Qin, Q.; Meng, J.; Zhao, S. A Practical Split-Window Algorithm for Estimating Land Surface Temperature from Landsat 8 Data. *Remote Sens.* **2015**, *7*, 647–665. [[CrossRef](#)]

23. Jiménez-Muñoz, J.C.; Cristobal, J.; Sobrino, J.A.; Soria, G.; Ninyerola, M.; Pons, X. Revision of the Single-Channel Algorithm for Land Surface Temperature Retrieval From Landsat Thermal-Infrared Data. *IEEE Trans. Geosci. Remote Sens.* **2009**, *47*, 339–349. [[CrossRef](#)]
24. Jin, M.; Li, J.; Wang, C.; Shang, R. A Practical Split-Window Algorithm for Retrieving Land Surface Temperature from Landsat-8 Data and a Case Study of an Urban Area in China. *Remote Sens.* **2015**, *7*, 4371–4390. [[CrossRef](#)]
25. Ru, C.; Duan, S.-B.; Jiang, X.-G.; Li, Z.-L.; Jiang, Y.; Ren, H.; Leng, P.; Gao, M. Land Surface Temperature Retrieval From Landsat 8 Thermal Infrared Data Over Urban Areas Considering Geometry Effect: Method and Application. *IEEE Trans. Geosci. Remote Sens.* **2022**, *60*, 5000716. [[CrossRef](#)]
26. Li, Y.; Liu, T.; Shokr, M.E.; Wang, Z.; Zhang, L. An Improved Single-Channel Polar Region Ice Surface Temperature Retrieval Algorithm Using Landsat-8 Data. *IEEE Trans. Geosci. Remote Sens.* **2019**, *57*, 8557–8569. [[CrossRef](#)]
27. Jiménez-Muñoz, J.C.; Sobrino, J.A.; Skokovic, D.; Mattar, C.; Cristobal, J. Land Surface Temperature Retrieval Methods From Landsat-8 Thermal Infrared Sensor Data. *IEEE Geosci. Remote Sens. Lett.* **2014**, *11*, 1840–1843. [[CrossRef](#)]
28. Key, J.R.; Collins, J.B.; Fowler, C.; Stone, R.S. High-latitude surface temperature estimates from thermal satellite data. *Remote Sens. Environ.* **1997**, *61*, 302–309. [[CrossRef](#)]
29. Key, J.R.; Mahoney, R.; Liu, Y.; Romanov, P.; Tschudi, M.; Appel, I.; Maslanik, J.; Baldwin, D.; Wang, X.; Meade, P. Snow and ice products from Suomi NPP VIIRS. *J. Geophys. Res. Atmos.* **2013**, *118*, 12816–12830. [[CrossRef](#)]
30. Fan, P.; Zhao, X.; Qu, M.; Yan, Z.; Chen, Y.; Liang, Z.; Pang, X. Evaluation of the relationships and uncertainties of airborne and ground-based sea ice surface temperature measurements against remotely sensed temperature records. *Int. J. Digit. Earth* **2022**, *15*, 1989–2005. [[CrossRef](#)]
31. Wulder, M.A.; Loveland, T.R.; Roy, D.P.; Crawford, C.J.; Masek, J.G.; Woodcock, C.E.; Allen, R.G.; Anderson, M.C.; Belward, A.S.; Cohen, W.B.; et al. Current status of Landsat program, science, and applications. *Remote Sens. Environ.* **2019**, *225*, 127–147. [[CrossRef](#)]
32. *Landsat 8 (L8) Data Users Handbook*; LSDS-1574 v.5.0; Department of the Interior U.S. Geological Survey, EROS: Sioux Falls, SD, USA, 2019. Available online: <https://www.usgs.gov/media/files/landsat-8-data-users-handbook> (accessed on 8 July 2023).
33. Kurtz, N.T.; Farrell, S.L.; Studinger, M.; Galin, N.; Harbeck, J.P.; Lindsay, R.; Onana, V.D.; Panzer, B.; Sonntag, J.G. Sea ice thickness, freeboard, and snow depth products from Operation IceBridge airborne data. *Cryosphere* **2013**, *7*, 1035–1056. [[CrossRef](#)]
34. Wan, Z.; Dozier, J. A generalized split-window algorithm for retrieving land-surface temperature from space. *IEEE Trans. Geosci. Remote Sens.* **1996**, *34*, 892–905.
35. Baldridge, A.M.; Hook, S.J.; Grove, C.; Rivera, G. The ASTER spectral library version 2.0. *Remote Sens. Environ.* **2009**, *113*, 711–715. [[CrossRef](#)]
36. Macander, M.J.; Swingley, C.S.; Joly, K.; Raynolds, M.K. Landsat-based snow persistence map for northwest Alaska. *Remote Sens. Environ.* **2015**, *163*, 23–31. [[CrossRef](#)]
37. Hall, D.K.; Riggs, G.A.; Salomonson, V.V. Development of methods for mapping global snow cover using moderate resolution imaging spectroradiometer data. *Remote Sens. Environ.* **1995**, *54*, 127–140. [[CrossRef](#)]
38. Hall, D.K.; Riggs, G.A.; Salomonson, V.V.; DiGirolamo, N.E.; Bayr, K.J. MODIS snow-cover products. *Remote Sens. Environ.* **2002**, *83*, 181–194. [[CrossRef](#)]
39. McFeeters, S.K. The use of the Normalized Difference Water Index (NDWI) in the delineation of open water features. *Int. J. Remote Sens.* **1996**, *17*, 1425–1432. [[CrossRef](#)]
40. Huang, C.; Chen, Y.; Zhang, S.; Wu, J. Detecting, extracting, and monitoring surface water from space using optical sensors: A review. *Rev. Geophys.* **2018**, *56*, 333–360. [[CrossRef](#)]
41. Yang, X.; Zhao, S.; Qin, X.; Zhao, N.; Liang, L. Mapping of urban surface water bodies from Sentinel-2 MSI imagery at 10 m resolution via NDWI-based image sharpening. *Remote Sens.* **2017**, *9*, 596. [[CrossRef](#)]
42. Barsi, J.A.; Barker, J.L.; Schott, J.R. An Atmospheric Correction Parameter Calculator for a single thermal band earth-sensing instrument. In Proceedings of the IGARSS 2003. 2003 IEEE International Geoscience and Remote Sensing Symposium. Proceedings (IEEE Cat. No.03CH37477), Toulouse, France, 21–25 July 2003.
43. Barsi, J.A.; Schott, J.R.; Palluconi, F.D.; Hook, S.J. Validation of a web-based atmospheric correction tool for single thermal band instruments. In Proceedings of the Earth Observing Systems X, San Diego, CA, USA, 22 August 2005.
44. Nielsen-Englyst, P.; Høyer, J.L.; Kolbe, W.M.; Dybkjær, G.; Lavergne, T.; Tonboe, R.T.; Skarpalezos, S.; Karagali, I. A combined sea and sea-ice surface temperature climate dataset of the Arctic, 1982–2021. *Remote Sens. Environ.* **2023**, *284*, 113331. [[CrossRef](#)]
45. Chen, H.; Meng, X.; Li, L.; Ni, K. Quality Assessment of FY-3D/MERSI-II Thermal Infrared Brightness Temperature Data from the Arctic Region: Application to Ice Surface Temperature Inversion. *Remote Sens.* **2022**, *14*, 6392. [[CrossRef](#)]

Disclaimer/Publisher’s Note: The statements, opinions and data contained in all publications are solely those of the individual author(s) and contributor(s) and not of MDPI and/or the editor(s). MDPI and/or the editor(s) disclaim responsibility for any injury to people or property resulting from any ideas, methods, instructions or products referred to in the content.